

Properties of the Simulated Circumgalactic Medium

Cassandra Lochhaas¹, Greg L. Bryan^{2,3}, Yuan Li³, Miao Li³, Drummond Fielding^{3,4}

¹ *Department of Astronomy, The Ohio State University, 140 West 18th Avenue, Columbus, OH 43210, USA*

² *Department of Astronomy, Columbia University, 550 West 120th Street, New York, NY 10027, USA*

³ *Center for Computational Astrophysics, Flatiron Institute, 162 5th Avenue, New York, NY 10010, USA*

⁴ *Department of Astronomy and Theoretical Astrophysics Center, University of California at Berkeley, 501 Campbell Hall #3411, Berkeley, CA 94720, USA*

14 September 2018

ABSTRACT

The circumgalactic medium (CGM) is closely linked to galaxy formation and evolution, but difficult to characterize observationally and typically poorly resolved in cosmological simulations. We use spherically-symmetric, idealized, high-resolution simulations of the CGM in $10^{12}M_{\odot}$ and $10^{11}M_{\odot}$ dark matter halos to characterize the gas pressure, turbulent and radial velocities, and degree of hydrostatic equilibrium in the overall CGM as well as in its high- and low-temperature phases. We find that the $10^{12}M_{\odot}$ halo contains a CGM mostly formed of a hot gas halo in hydrostatic equilibrium out of which cold gas condenses and falls onto the central galaxy, while the $10^{11}M_{\odot}$ halo’s CGM is not in hydrostatic equilibrium, is highly time-variant, does not have a clear separation of hot and cold phases, and is dominated by bulk motions of gas. We also find that the degree of pressure support in the $10^{11}M_{\odot}$ halo is strongly dependent on the parameters of the galactic winds of the central galaxy. These results promote the idea that there is no “average” CGM and care must be taken when setting the initial conditions for a small-box simulation of a patch of the CGM.

Key words: galaxies: haloes

1 INTRODUCTION

The circumgalactic medium (CGM) is the conduit between galaxies and the intergalactic medium, through which all gas that flows into or out of a galaxy must pass (see Tumlinson et al. 2017, for a recent review). Observations have indicated that the CGM contains a significant amount of mass, as much or more as the mass in the galactic disk (Peeples et al. 2014; Werk et al. 2014; Keeney et al. 2017), and that it is multiphase with a variety of different temperatures and densities (e.g., Gupta et al. 2012; Tumlinson et al. 2013; Bordoloi et al. 2014; Borthakur et al. 2015). The large mass and close location of the CGM to the galaxies that host it indicate it is closely linked to the growth and evolution of galaxies, yet there are many open questions about the processes governing it.

Due to the diffuse nature of the CGM, it is difficult to characterize the CGM observationally. Typical surveys of the full extent of the CGM probe diffuse X-ray emission (Anderson & Bregman 2010; Anderson et al. 2013) or require spectra of background quasars and obtain just a handful of lines of sight through a given galaxy’s CGM (Rudie et al. 2012; Tumlinson et al. 2013; Bordoloi et al. 2014; Borthakur et al. 2015; Keeney et al. 2017) and are limited in prob-

ing the full structure. Instead, simulations can provide additional insight into not just the statistical properties of the CGM, but also some understanding of its physical structure and evolution. Fully cosmological simulations do not have high enough resolution to resolve the CGM, and cosmological zoom-in simulations (Anglés-Alcázar et al. 2014; Hopkins et al. 2014; Rahmati et al. 2016; Henden et al. 2018; Pillepich et al. 2018) typically refine the densest regions, the galaxies, while the diffuse CGM remains poorly resolved. Simulations specifically designed to study the CGM are needed (Sarkar et al. 2015; Fielding et al. 2017).

Simulations of thermal instability have found that cold gas condenses out of a hot medium if the cooling time is short compared to the dynamical time of the gas (McCourt et al. 2012; Sharma et al. 2012; Voit et al. 2017; Voit 2018). Such instability could be a source of the cool phase of gas in the CGM, but extremely high-resolution simulations are necessary to resolve the cooling length. The CGM extends to the dark matter halo virial radius, hundreds of kiloparsecs for massive galaxies, so resolving the entirety of the CGM at the level required to fully track condensation is computationally expensive. Small-box simulations of just a small

region of a galactic wind flow or the CGM (Ferrara & Scannapieco 2016; Gronke & Oh 2018; Liang & Remming 2018) can reach the resolution needed to track cooling condensation, but they must be initialized with certain properties that represent a realistic CGM, such as a general gas pressure or turbulent and outflowing velocities. Full-CGM simulations, while not high enough resolution to resolve the coldest clouds, are necessary for providing the overall properties of the CGM that can be used for initializing small-box simulations. In addition, idealized simulations of the CGM are useful for understanding the bulk physics affecting the gas.

In this paper, we aim to quantify not just the overall mean properties of the simulated CGM, but also the spatial, temporal, and statistical fluctuations of the gas. Understanding the physical processes that produce and govern all parts of the multiphase gas, not just the majority of it, provides the specificity needed for initializing small-box CGM simulations and provides a basis from which to interpret observations that trace different phases of gas. We base our analysis on the simulations of Fielding et al. (2017), which are high-resolution, 3D, idealized, isolated galaxy simulations.

In §2, we give a brief overview of the simulations used and how we analyze them. Section 3 presents our findings of how pressures and velocities vary at a given radius (§3.1), and of how the pressure (§3.2), velocity (§3.3), turbulence (§3.4), and balance of hydrostatic equilibrium (§3.5) vary with galactocentric radius and fluctuate at a given radius. We discuss the picture of how the CGM changes with halo mass (§4.1), the impact of our results (§4.2) and how they vary with the implementation of the galactic wind (§4.3) in §4, and summarize and give conclusions in §5.

2 SIMULATIONS AND ANALYSIS

We use the simulations of Fielding et al. (2017), and refer the reader to that study for more details but give an overview of the simulations here. These simulations are 3D hydrodynamic simulations using the ATHENA code that do not model the galaxy nor cosmological structure. They have static mesh refinement so that the region closest to the galaxy at the center of the domain has higher resolution than the outskirts of the CGM; the resolution varies from ~ 1 kpc close to the galaxy to ~ 5 kpc at the outer edge of the domain, past the virial radius of the halo. They are spherically symmetric, with the inner edge of the domain at small radius representing the (spherical) galaxy. The only gravity included is that of a NFW (Navarro et al. 1997) dark matter halo.

Both the inner edge and the outer edge allow inflows and outflows — at the outer edge, there is spherical cosmological accretion at a rate of $\dot{M}_{\text{acc}} = 7M_{\odot} \text{ yr}^{-1} (M_{\text{halo}}/10^{12}M_{\odot})$, where M_{halo} is the mass of the dark matter halo. At the inner edge, gas from the CGM can fall onto the galaxy, and feedback in the form of galactic winds are injected (spherically) back out of the galaxy. The mass outflow rate of winds is related to the rate at which mass falls onto the galaxy (i.e. through the inner edge of the simulated domain) by

$$\dot{M}_{\text{out}} = \frac{\eta}{\eta + 1} \dot{M}_{\text{in}}, \quad (1)$$

where η is the mass-loading factor of the wind and is set to a constant value for the duration of the simulation. The winds are also parameterized by the injection velocity, v_w , which is set to a constant value proportional to the escape speed from the galaxy, v_{esc} , for the duration of the simulation. At the inner edge of the domain, where the wind is launched, $v_{\text{esc}} \approx 3.5v_{\text{vir}}$ where v_{vir} is the virial velocity of the halo. The wind is blowing for the full duration of the simulations.

The metallicity of the gas is fixed to one-third solar, and is the same for both the accreting gas and the galactic outflows. Outflows are expected to be metal-enriched compared to mostly-pristine cosmological accretion (Muzahid et al. 2015; Chisholm et al. 2018; Christensen et al. 2018), so this fixed metallicity is an idealized simplification. However, many CGM studies find a metallicity $\sim 0.3Z_{\odot}$ (Prochaska et al. 2017; Muzahid et al. 2018). The gas is assumed to be in optically-thin photoionization equilibrium from a Haardt & Madau (2001) ionizing background. The gas is allowed to radiatively cool, but there is a cooling floor of $T = 10^4$ K, the temperature expected for photoionized gas, to prevent runaway unresolved cooling. The simulations are initialized with virial shocks within which the gas is isothermal, and there are isobaric density perturbations throughout the simulation domain that break the spherical symmetry.

We focus on two simulations for the majority of this paper. The first, which has a larger dark matter halo mass, has $M_{\text{halo}} = 10^{12}M_{\odot}$, mass-loading $\eta = 2$, wind speed $v_w^2 = 3v_{\text{esc}}^2$, virial velocity $v_{\text{vir}} = 116 \text{ km s}^{-1}$, and virial radius $R_{\text{vir}} = 319$ kpc (the $10^{12}M_{\odot}$ simulation labeled “fiducial high η ” in Table 1 of Fielding et al. (2017)). The inner edge of the domain is a sphere of radius 8 kpc, representing the galaxy. The outer edge of the domain is a sphere of radius $2R_{\text{vir}} = 638$ kpc. The second, lower-mass halo, has $M_{\text{halo}} = 10^{11}M_{\odot}$, mass-loading $\eta = 5$, wind speed $v_w^2 = 3v_{\text{esc}}^2$, virial velocity $v_{\text{vir}} = 54 \text{ km s}^{-1}$, and virial radius $R_{\text{vir}} = 148$ kpc (the $10^{11}M_{\odot}$ simulation labeled “strong high η ” in Table 1 of Fielding et al. (2017)). The inner edge of this simulation domain is a sphere of radius 3.7 kpc and the outer edge is a sphere of radius 296 kpc. We pick these two simulations to explore the changes of the CGM with halo mass, and these wind parameters are most representative of the observed winds from galaxies of these sizes (Heckman et al. 2015; Muratov et al. 2015).

To perform our analysis of the simulated CGM, we first chose 14 snapshots in time for each simulation, starting at 0.7 Gyr and ending at 9.8 Gyr, separated by 0.7 Gyr. At each snapshot, we split the full simulation domain into 3D radial bins. Our CGM gas parameters of interest are the density, temperature, thermal pressure, spherical velocity components, and turbulent pressure. Using the python simulation analysis and visualization module yt (Turk et al. 2011), we computed a histogram (normalized by either mass or volume, depending on the parameter) of the values of parameters of interest of all cells that fall into each radial bin at that given time snapshot, then compute the median and interquartile range (IQR) representing the 20% to 80% interval of either mass or volume, depending on parameter, of all cells in the bin. We then averaged the histograms, medians, and IQRs over time and found the standard deviation of these values in time as well. In this way, the median value of a parameter in a radial bin represents the time-averaged value of the majority of the gas in the bin, and the IQR

represents the time-averaged range of values of all gas in a given radial bin. The standard deviation on these parameters represents only the fluctuation in time.

3 RESULTS

3.1 Histograms in Radial Bins

The density, temperature, and pressure of the CGM gas is a natural place to start characterizing the overall CGM. It is well-known observationally that the CGM and galactic winds are both multiphase, with gas ranging from 10^2 K to 10^{7-8} K in temperature and similarly as many orders of magnitude in density (see Tumlinson et al. 2017, for a recent review). In addition, the peak of the radiative cooling curve near 10^5 K allows warm gas to cool to 10^4 K rapidly, so a multiphase medium is expected to form from thermal instability as cool gas precipitates out of the warm/hot medium. The multiphase nature of the CGM is clearly evident in histograms of density and temperature in radial bins (not shown) — even when considering gas all located at the same radius, the histograms of density or temperature are not well-described by a normal distribution. Instead, we see that the bulk of the gas is located at a characteristic density or temperature, but there is a tail of the distribution toward low temperature and high density. Due to this non-symmetric shape of the histogram for density and temperature, the median and IQR are not good descriptors of the distribution. We direct the reader to Fielding et al. (2017) for the time-averaged density and temperature radial distributions (their Figure 7, see also Figure 11 for the density radial distribution in temperature bins) and histograms of the density in radial bins (their Figure 10) for these simulations.

3.1.1 Thermal Pressures

Here, we focus instead on the thermal pressure histograms in radial bins. Unlike the density and temperature, the thermal pressure histograms are visually closer to log-normal distributions, so we characterize them with a median and IQR. Figure 1 shows histograms of the thermal pressure (solid black curves) in each radial bin for the $M_{\text{halo}} = 10^{12} M_{\odot}$ simulation, where the histogram is calculated over the volume. At both small and large radii, the pressure distribution departs from a single log-normal and becomes bimodal. At large radii, the bimodal pressure distribution is due to the fact that part of the radial bin lies within the virial shock and part lies outside of it. As gas passes through the virial shock, it is significantly heated and pressurized above its original cold, low-pressure accretion state. At small radii, the CGM is dominated by a number of wind shocks as the galactic wind propagates out of the galaxy, which also creates a bimodal pressure distribution as the wind is heated by passing through shocks. The shading indicates one standard deviation of the histogram’s time variance, and an inclusion of zero volume within the shading indicates that one standard deviation of the time variance includes histograms that do not contain any cells at the range of pressures covered by the shading that reaches zero. For all but the smallest radial bin, the second peak of the bimodal distribution, for those

radial bins that show a bimodal distribution, has shading that reaches down to zero normalized volume. This means that the second peak of the distribution is not well-defined over time, and may not exist for many of the time snapshots considered. Therefore, it is a transient feature of the pressure distribution in any given radial bin, while the other peak (at larger pressure) in those distributions that are bimodal, which does not have shading that extends to zero, is time-invariant.

Figure 2 shows the histograms of thermal (solid black) and turbulent (dashed green) pressures in radial bins in the simulation with $M_{\text{halo}} = 10^{11} M_{\odot}$. Note that the radial bins are different here due to the smaller size of this halo. Like the larger mass halo, we again see some weak signatures of bimodality in the histograms at small and large radius, and again the second, weaker peak has a larger time variance, as evidenced by the shading around the second peak (which indicates one standard deviation of the histogram’s time variance) reaching zero normalized volume. Compared to the larger-mass halo, the thermal pressure histograms are wider, even if only the dominant peak of the distribution is considered. This indicates that at a given radius, the lower-mass halo contains gas that is less-uniform in pressure than the higher-mass halo. In addition, the peak of the pressure histograms are located at a lower pressure than the higher-mass halo, which is to be expected because the virial temperature of the lower-mass halo is significantly lower, so it is initialized with a lower-temperature CGM.

3.1.2 Velocities

Because the CGM is the site of both galactic outflows and cosmological accretion flows, it is also natural to consider the velocity of the gas as a defining characteristic of the CGM. We split the velocity of the gas into the 3D spherical velocity components: radial velocity v_r , velocity in the θ direction v_{θ} , and velocity in the ϕ direction v_{ϕ} . These simulations are spherically symmetric without rotation, so we do not expect any systematic differences between v_{θ} and v_{ϕ} . However, due to the outflows and accretion both being injected spherically at the inner and outer edges of the domain, respectively, we do expect v_r to vary significantly from either of the other velocity directions. We plot the three components of velocity in the larger-mass halo as histograms, normalized by mass (different from the pressure histograms, which were normalized by volume), within the same radial bins as above, in Figure 3. The radial velocity is plotted as the solid black curve, and the v_{θ} and v_{ϕ} velocities are plotted as the green dashed and magenta dotted curves, respectively. Shaded regions around the curves indicate the one standard deviation variance of the histograms over the 14 time snapshots, as above.

The v_{θ} and v_{ϕ} histograms are essentially equivalent in all radial bins, as expected. They are also well-described as log-normal distributions with no significant tails to either high or low velocity. There is some time variance in the width of the distribution, as evidenced by wide shading at the wings of the histogram, but the location of the peak is strongly time-invariant. The width of the v_{θ} and v_{ϕ} distributions decreases with increasing galactocentric radius. Because the velocities in these directions do not contain any information about outflows or inflows (the histograms are

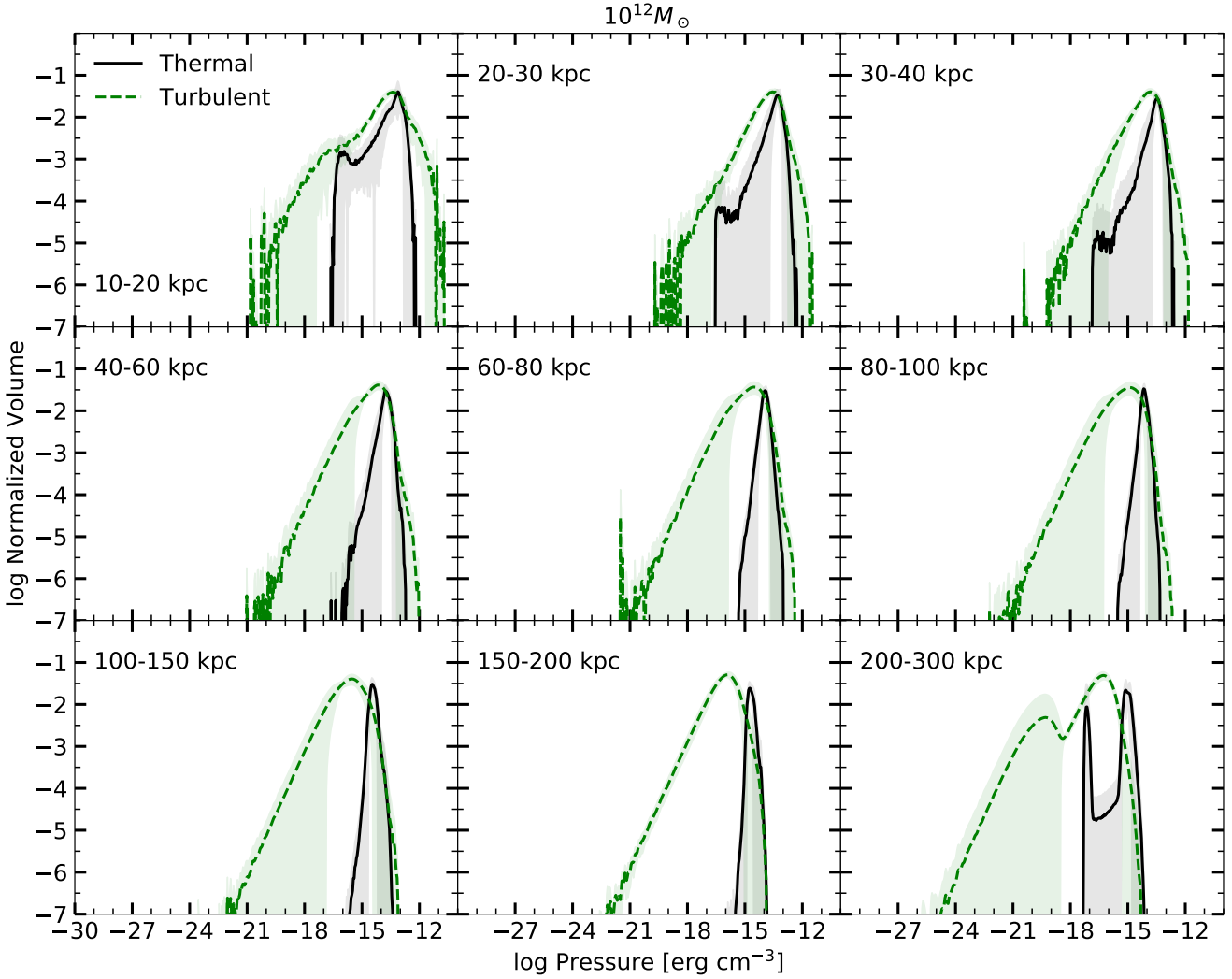


Figure 1. Volume histograms of the thermal (solid black) and turbulent (dashed green) pressure in radial bins in the $M_{\text{halo}} = 10^{12} M_{\odot}$ simulation. The histograms are averaged over the 14 time snapshots linearly spread between 0.7 Gyr and 9.8 Gyr, and the shading shows one standard deviation of the histograms’ variation with time.

centered at 0 km s^{-1} in every radial bin), and because they are equivalent to each other, they trace the turbulent velocity in each radial bin. The turbulence may be seeded by the inflows and outflows, but it is clear that it becomes isotropic in the directions where there are no bulk flows.

The v_r histogram shows a large difference from the v_{θ} and v_{ϕ} histograms. This is expected, as the v_r component of the velocity includes the outflows and inflows that have no significant velocities in the angular directions. The outflow is evident in the radial velocity histogram as a long and time-variant tail to positive velocities, which extends to higher velocities at smaller radii. Most notable at small radii, there is also a signature of inflow that appears as a small “bump” in the histogram at negative velocities. In addition to the bulk flows, there is likely also a component of turbulence in v_r . The equivalent histograms of v_{θ} and v_{ϕ} centered at 0 km s^{-1} show the turbulence is isotropic in those directions, so the v_r distribution may also contain a component of turbulence in the radial direction. However, this is difficult to separate from the bulk flows. Assuming that the turbulence in the

radial direction is the same as the turbulence in the angular directions, the v_{θ} or v_{ϕ} histogram could be subtracted from the v_r histogram to isolate just bulk flows. In doing so, we see that there is a signature of inflow in all radial bins, not just the smallest, which is evidenced by the small excess of v_r over v_{θ} or v_{ϕ} at negative velocities. In the largest radial bin, the v_r distribution is strongly bimodal. This is again because this bin straddles the virial shock, outside of which there is no outflowing gas, only inflowing.

Figure 4 shows the velocity histograms in radial bins for the lower-mass halo. Again, we see v_{θ} and v_{ϕ} trace turbulence, as their distributions are again equivalent and centered on 0 km s^{-1} , as well as being fairly time-invariant. In this lower-mass halo, the width of the turbulence distributions are narrower, which is expected if the bulk radial flows seed the turbulence because the outflows have a lower velocity by design than the $10^{12} M_{\odot}$ halo. The width of the v_{θ} and v_{ϕ} distributions do not narrow with increasing radius as strongly as the higher-mass halo. Again, the v_r distribution shows outflows at positive velocity, inflows as a “bump” at

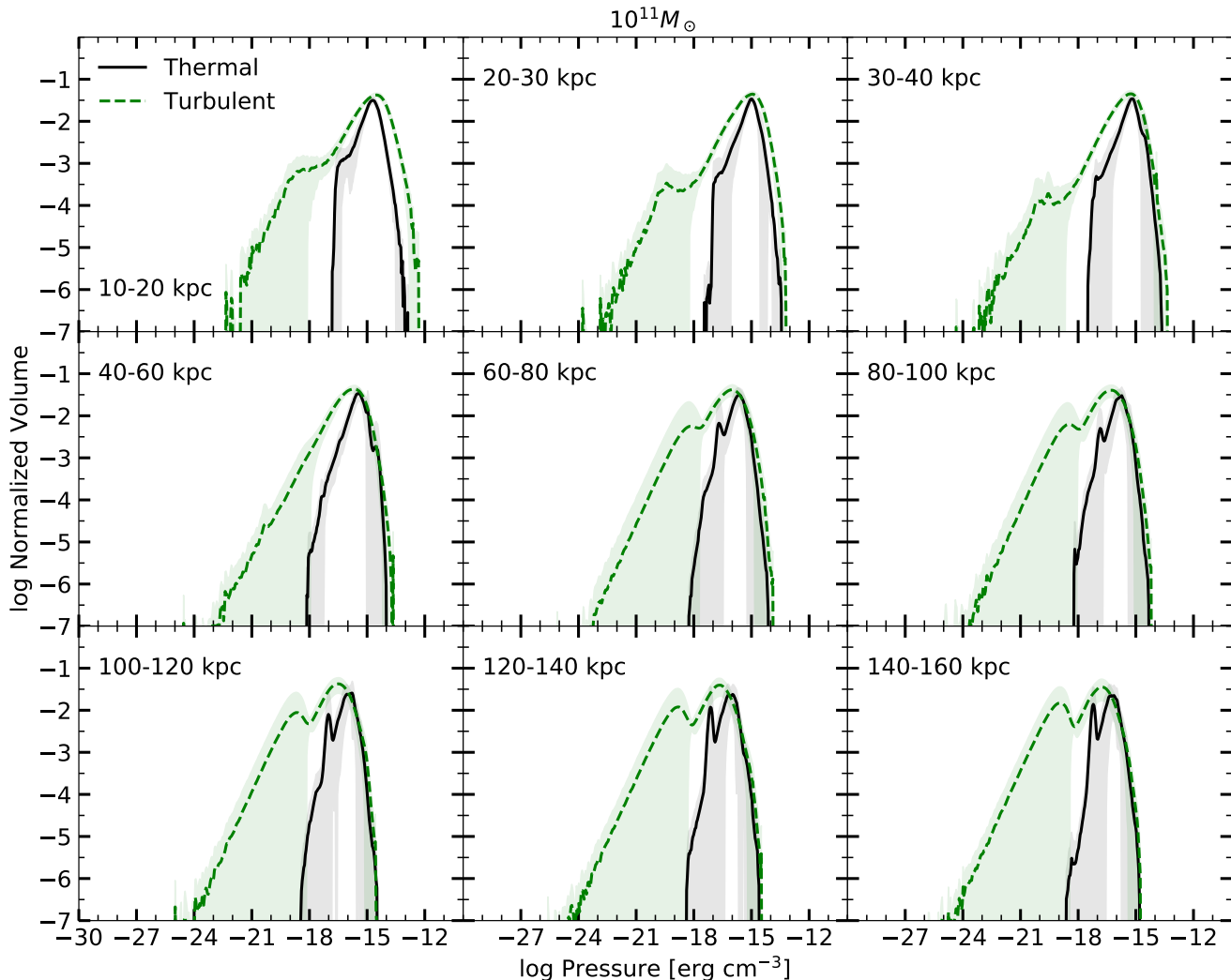


Figure 2. Same as Figure 1, but for the lower-mass halo. Volume histograms of the thermal (solid black) and turbulent (dashed green) pressure in radial bins in the $M_{\text{halo}} = 10^{11} M_{\odot}$ simulation. The histograms are averaged over the 14 time snapshots linearly spread between 0.7 Gyr and 9.8 Gyr, and the shading shows one standard deviation of the histograms' variation with time.

negative velocity, and likely contains a turbulence component equivalent to the v_{θ} or v_{ϕ} distributions. This halo is somewhat more inflow-dominated than the lower-mass halo: the excess in the v_r histogram over v_{θ} or v_{ϕ} at negative velocities is slightly more than the excess in the higher-mass halo. There is also a more significant bimodality of the v_r distribution than in the higher-mass halo, with a second very narrow and highly time-variant peak at negative velocities. This is due to the simulation developing significant spherical asymmetries in the outer regions of its CGM that are highly time-variant. The outflow follows the path of least resistance through the halo, so when a higher-density region develops, it is dominated by inflow while the outflow pushes through a lower-density region in a different direction. The presence of both large inflowing clumps and outflowing bubbles at different azimuthal directions in the same radial bin produces the bimodal shape of the histogram.

3.1.3 Turbulent Pressure

We use the v_{θ} and v_{ϕ} histograms to trace the turbulence in the simulations, and we can calculate the turbulent pressure as $P_{\text{turb}} = \rho v_t^2$, where $v_t^2 = v_{\theta}^2 + v_{\phi}^2 + v_{r,\text{turb}}^2$ is the turbulent velocity and $v_{r,\text{turb}}$ is the turbulent component of the radial velocity. Because the radial velocity is also affected by outflows and inflows, we cannot actually compute how much of a given cell's radial velocity is contributed by turbulence or bulk flows. Instead, we use the fact that the v_{θ} and v_{ϕ} histograms are equivalent to assume the turbulent velocity component of v_r is given by either the v_{θ} or v_{ϕ} distributions, and simply calculate $v_t^2 = \frac{3}{2}(v_{\theta}^2 + v_{\phi}^2)$, where we assume the average of v_{θ} and v_{ϕ} represents the turbulent velocity in any of the three spherical directions, which are then summed together in quadrature to obtain v_t^2 .

The volume histograms of this turbulent pressure is also plotted in Figure 1 for the larger-mass halo and Figure 2 for the lower-mass halo as the green dashed curves. Like the thermal pressure, the turbulent pressure histograms also show some signature of bimodality in the smallest and

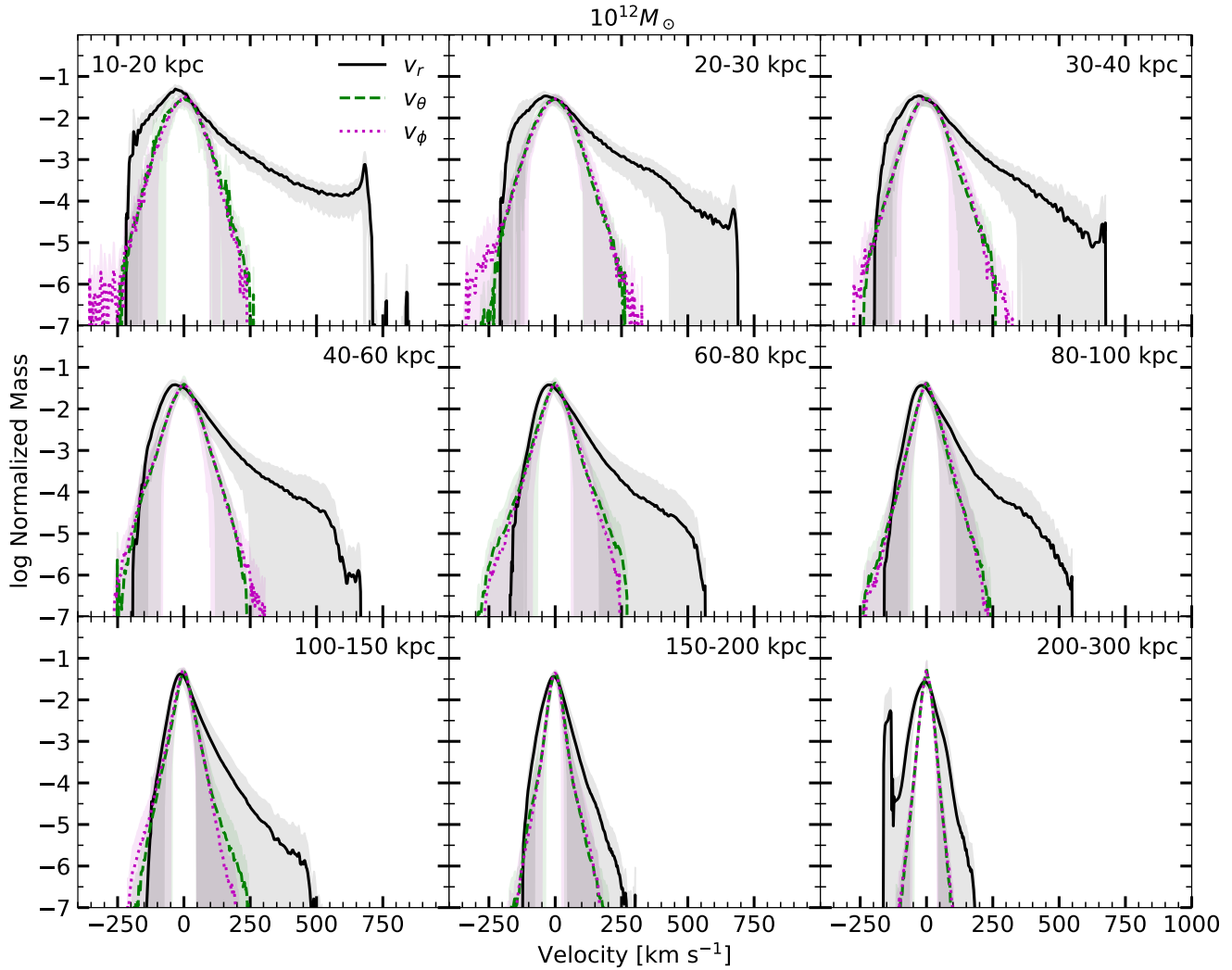


Figure 3. Mass histograms of the three components of spherical velocity, radial velocity v_r (black solid), v_θ (green dashed), and v_ϕ (magenta dotted) in radial bins in the $M_{\text{halo}} = 10^{11} M_\odot$ simulation. The histograms are averaged over the 14 time snapshots linearly spread between 0.7 Gyr and 9.8 Gyr, and the shading shows one standard deviation of the histograms' variation with time.

largest radial bins, also with significant time variance for the weaker secondary peak that indicates that peak is not present at every time snapshot. The lower-mass halo shows stronger bimodality in the turbulent pressure distributions than the higher-mass halo, just like for the thermal pressure. Because the turbulent velocity distribution is not bimodal (see Figure 3), the bimodality in the turbulent pressure must be due to a bimodality in the density of the gas, the other component of the turbulent pressure. Even when there is no bimodality in the turbulent pressure distribution, the histogram is not perfectly a log-normal distribution; there is what appears to be a power-law tail to lower pressure that is highly time-variant, present in both halos.

For both halos, the turbulent pressure distribution is wider than the thermal pressure distribution, and peaked at slightly lower pressures. When a bimodal distribution is present in one type of pressure, it is also present in the other, and both peaks of the turbulent pressure distribution are shifted to smaller pressures than both peaks of the thermal pressure distribution. The slightly lower pressure values of

the turbulent pressure than the thermal pressure indicate the thermal pressure is more important for supporting the gas against gravity in hydrostatic equilibrium than the turbulent pressure, a point we will return to in §3.5.

3.2 Radial Pressure Distributions

To examine how the global properties of the CGM change with galactocentric radius, we compute the median and interquartile range of the middle 60% of the volume histograms of both thermal and turbulent pressure, and then average these over the 14 time snapshots. Figure 5 shows the median thermal (filled black symbols) and turbulent (open green symbols) pressures as functions of radius (left panel) and the IQR of the pressure histograms (right panel), for both the $10^{12} M_\odot$ halo (circles) and the $10^{11} M_\odot$ halo (triangles). The shaded region around each curve shows one standard deviation of the time variance of the median and IQR.

Both halos show smoothly decreasing median thermal

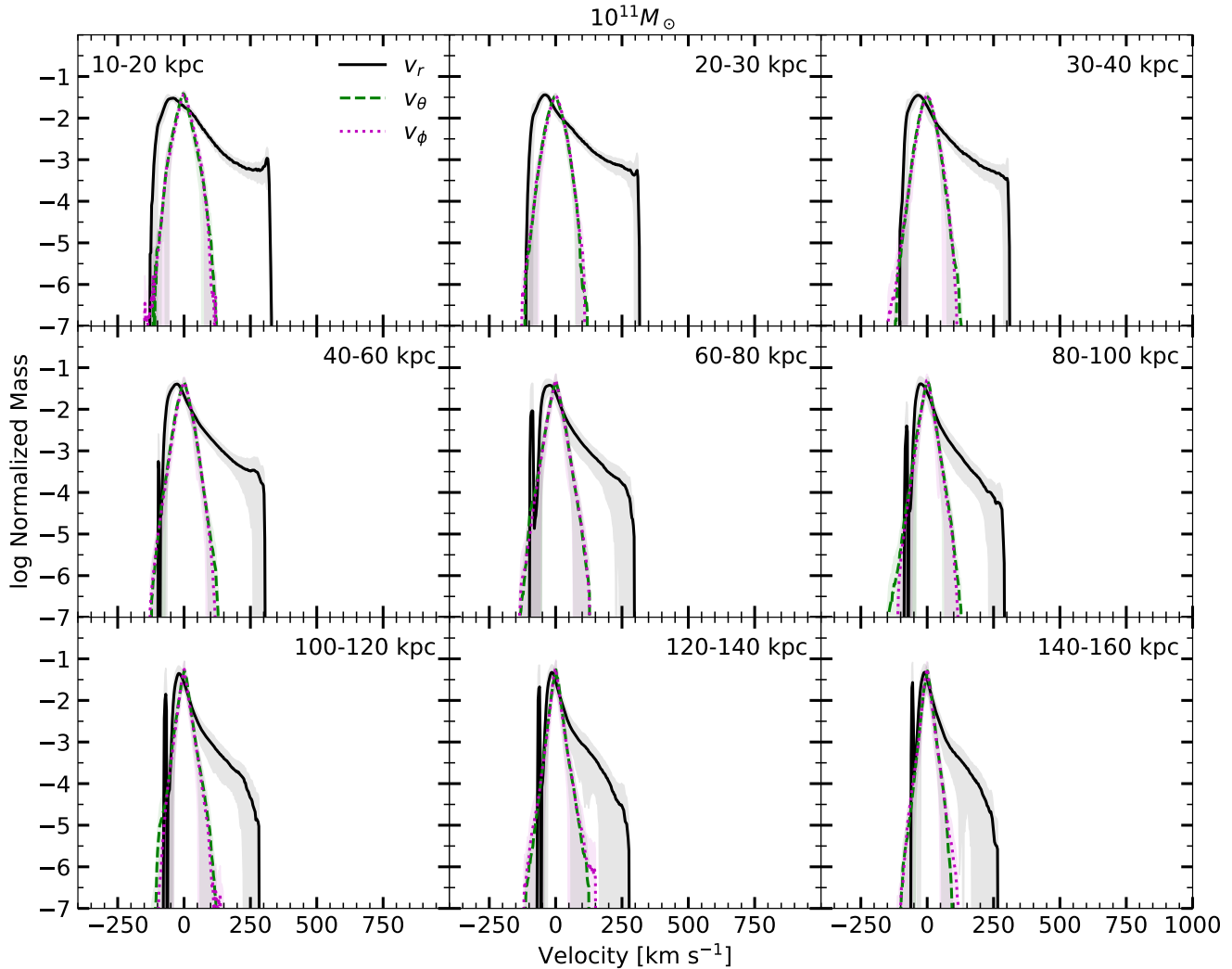


Figure 4. Same as Figure 3, but for the lower-mass halo. Mass histograms of the three components of spherical velocity, radial velocity v_r (black solid), v_θ (green dashed), and v_ϕ (magenta dotted) in radial bins in the $M_{\text{halo}} = 10^{11} M_\odot$ simulation. The histograms are averaged over the 14 time snapshots linearly spread between 0.7 Gyr and 9.8 Gyr, and the shading shows one standard deviation of the histograms’ variation with time.

and turbulent pressures with increasing radius, but both types of pressure in the higher-mass halo have larger values than both pressures in the lower-mass halo. For both halos, the thermal pressure is nearly always larger than the turbulent pressure, with the exception of the smallest radial bin for the lower-mass halo, where the turbulent pressure is slightly larger than the thermal. The higher-mass halo has a much smaller time variation in its median thermal pressure than its turbulent pressure, and than the thermal pressure in the lower-mass halo. In the $10^{11} M_\odot$ halo, the time variation in the turbulent pressure is somewhat smaller than the variation in its thermal pressure, which is opposite from the higher-mass halo. In the inner regions of both halos, the thermal and turbulent pressures are much closer in value than in the outskirts of the halo, where the thermal pressure can be 1 – 1.5 orders of magnitude larger than the turbulent pressure.

The IQR of the thermal pressure in the higher-mass halo is smaller, indicating a narrower distribution in a given

radial bin, than the lower-mass halo, but both are fairly constant with radius except for the innermost and outermost radial bins. The turbulent pressure’s IQR is larger than the thermal pressure’s by a little over half a dex for both halos, but is also constant with radius outside of the innermost radius bins. Despite the lower-mass halo having a larger IQR of thermal pressure than the higher-mass halo at nearly all radii, the turbulent pressures’ IQRs in both halos consistent with each other, within one standard deviation of the time variance.

Figure 5 indicates that the higher-mass halo’s thermal pressure is very well-behaved: it varies smoothly with galactocentric radius, does not have large time variation, and has small IQRs. The thermal pressure in the lower-mass halo, by contrast, has a larger time-variance (although it is also smoothly varying with galactocentric radius), and has a larger IQR, possibly indicating that the lower-mass halo is not as pressure-regulated as the higher-mass halo. For both halos, the turbulent pressure has a larger IQR than

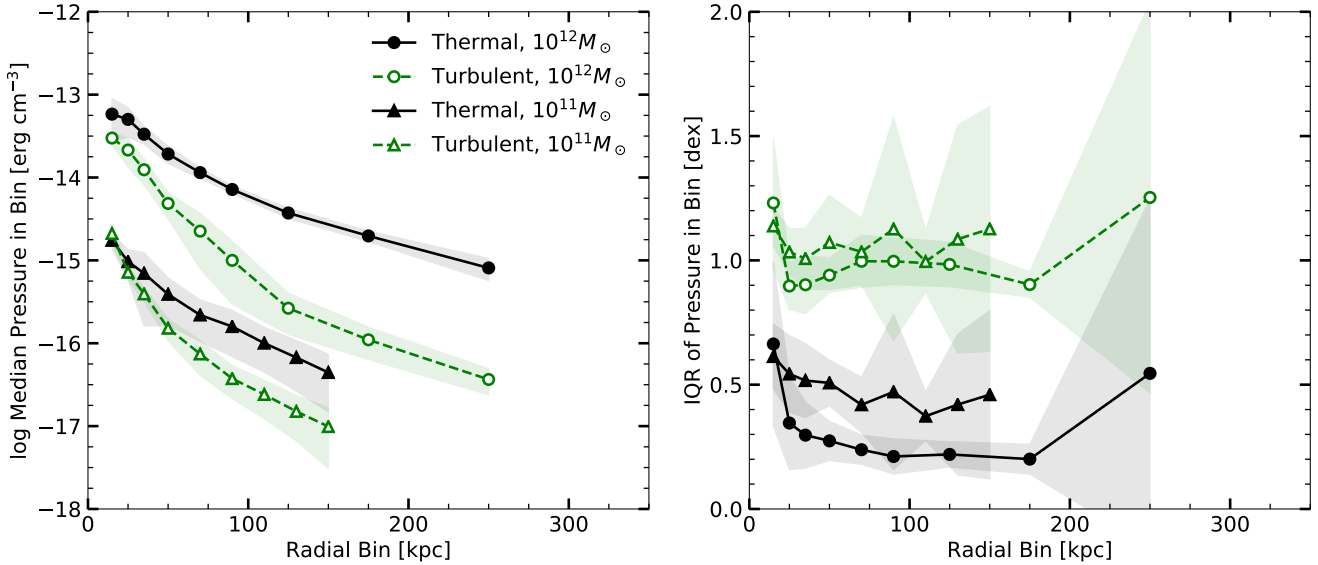


Figure 5. Left panel shows the time-averaged median thermal (black filled symbols) and turbulent (open green symbols) pressures as functions of radius for both the $10^{12}M_{\odot}$ (circles) and $10^{11}M_{\odot}$ halos. Right panel shows the time-averaged IQR for both types of pressure in both halos. Shaded regions around curves indicate the one standard deviation time variance of the values.

the thermal pressure, indicating that there is not a consensus on turbulent pressure support of all gas within a radial bin, and the turbulent pressure is not as strong as the thermal pressure.

3.3 Radial Velocity Distributions

The higher-mass halo’s pressure distributio is well-regulated, so the gas in this halo may be supported by thermal pressure. However, the lower-mass halo has a larger variance in its thermal pressure, and neither halo’s turbulent pressure is strong compared to the thermal pressure, so we next turn to the velocity distributions to investigate a separate source of support for the CGM gas. Figure 6 shows the time-averaged median (left panels) and IQR (right panels) of the radial velocity histograms in each radial bin, for both halos ($10^{12}M_{\odot}$: circles, $10^{11}M_{\odot}$: triangles). The top panels show the radial velocities of all gas in each simulation, while the bottom panels show the median and IQR of radial velocity histograms containing only the hot gas at $T > 10^{4.7}$ K (filled symbols, red for higher-mass halo and orange for lower-mass halo) or only the cold gas at $T < 10^{4.7}$ K (open symbols, dark blue for higher-mass halo and light blue for lower-mass halo).

Considering the top-left panel of Figure 6 first, both halos are inflow-dominated because the median of the radial velocity histograms in each radial bin is negative, as we saw previously in Figures 3 and 4, where the peaks of the radial velocity histograms were negative. The lower-mass halo has slightly more negative median radial velocities at all radial bins than the higher-mass halo, indicating that this halo is slightly more inflow-dominated. There is a very weak trend of increasing median radial velocity with increasing galactocentric radius in both halos. The median radial velocity is much more time-variant in the lower-mass halo than in the higher-mass halo.

The top-right panel of Figure 6 shows that the spread of radial velocities within a given radial bin is larger in the

higher-mass halo than in the lower-mass halo. This is expected, as the outflows are faster in the higher-mass halo than in the lower-mass halo, thus broadening the histogram in a given radial bin. For both halos, the width of the radial velocity histogram decreases with increasing radius (except for the largest radial bin in the higher-mass halo) because the outflows slow down as they reach larger distances from the galaxy. Both halos have similar IQR time variance, despite the fact that the higher-mass halo has a smaller time-variance in the median radial velocity. This means that the bulk of the gas in the higher-mass halo has a fairly constant (slowly inflowing) velocity, but the high-speed outflows, that pull the histograms wider, are more time-variable. The lower-mass halo is more time-variable in the radial velocity of the bulk of the gas (as shown by the wider standard deviation on the median), but has similar time-variance in the high-speed outflows as the higher-mass halo.

The similarities between the halos vanish when the gas is split into high-temperature ($T > 10^{4.7}$ K) and low-temperature ($T < 10^{4.7}$ K) before the histograms and their medians and IQRs are computed. We choose $10^{4.7}$ K as the dividing temperature because this temperature separates the bimodal phase distributions of all gas in the simulations well for both the higher-mass and the lower-mass halos (see Figure 8 in Fielding et al. (2017) for the temperature of all mass in the simulations over time). Note, however, that the gas with temperature above $10^{4.7}$ K in the higher-mass halo is higher temperature than the gas above this dividing line in the lower-mass halo, and the division between the two gas temperatures is more distinct in the higher-mass halo than in the lower-mass halo, especially at later times in the simulations. Considering the lower-left panel of Figure 6, the median radial velocities of the gas above (red filled) and below (dark blue open) the dividing temperature in the higher-mass halo (circles) are clearly separated. The hot gas is still dominated by inflow, but at much slower inflowing velocities

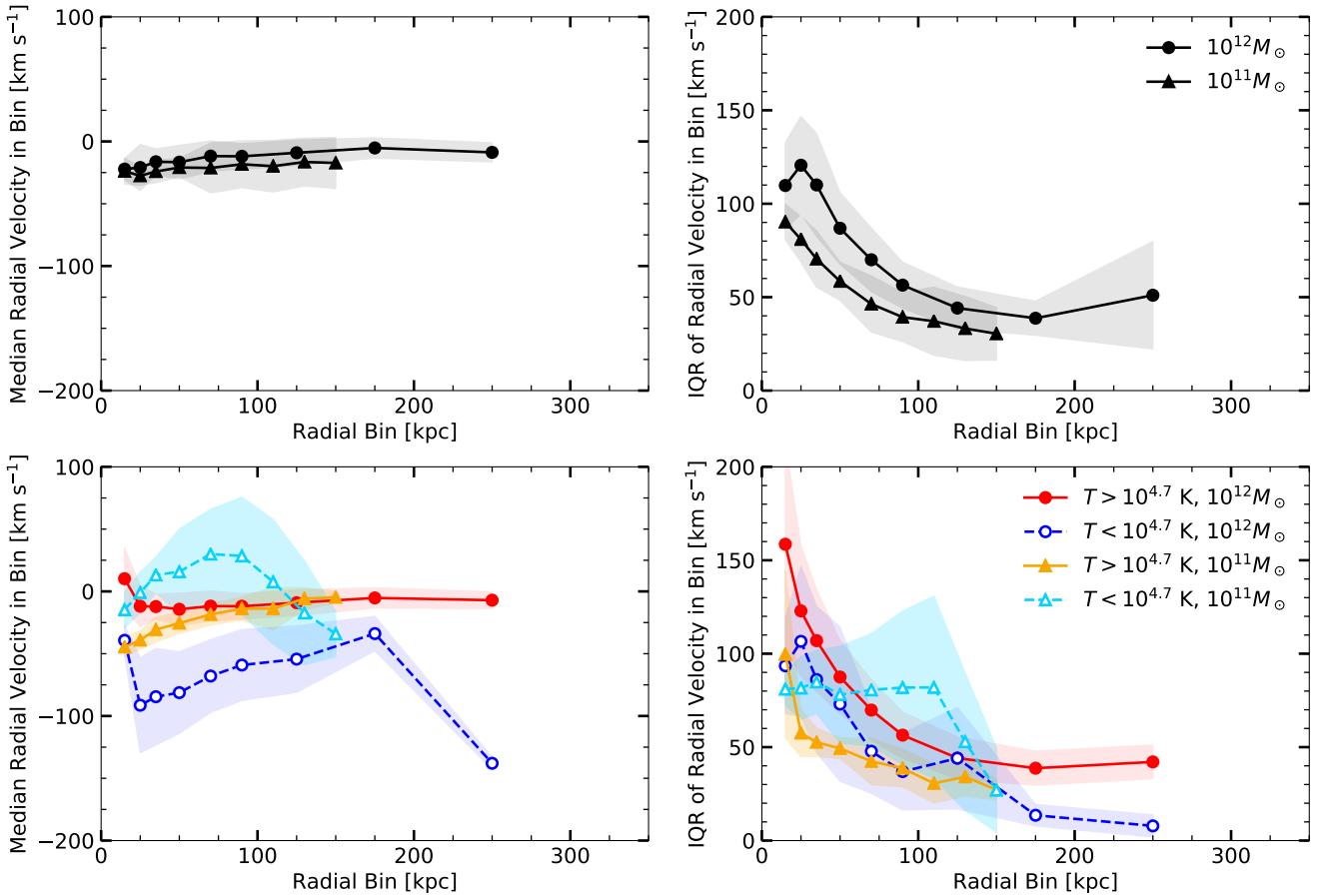


Figure 6. Left panels show the time-averaged median radial velocity as a function of radius for both the $10^{12}M_{\odot}$ (circles) and $10^{11}M_{\odot}$ halos. Right panels show the time-averaged IQR of the radial velocity histograms in both halos. Top panels show radial velocities for all gas in each simulation, while bottom panels show the median and IQR of the radial velocity histograms when the gas is first separated by temperature at $T = 10^{4.7}$ K. Shaded regions around curves indicate the one standard deviation time variance of the values. Note that the values in the top panels are the averages of the bottom panels only when weighted by the mass of gas in each temperature phase.

$\sim 10 \text{ km s}^{-1}$ than the cold gas, which has inflowing velocities $\sim 50 - 100 \text{ km s}^{-1}$. The median velocity of the hot gas is also much less time-variable than that of the cold gas. In the lower-mass halo, the median radial velocities of the hot and cold gases are flipped such that the cold gas has a median velocity closer to zero or even positive, indicating outflow, in most radial bins, while the hot gas is more quickly inflowing in most radial bins. Unlike in the higher-mass halo, the lower-mass halo’s hot and cold gas median velocities cross each other at large radius, where the hot gas has a radial velocity of $\sim 0 \text{ km s}^{-1}$ and the cold gas has a radial velocity more strongly negative. For both halos, the hot gas’s radial velocity is less time-variant than the cold gas’s.

Finally, the bottom-left panel of Figure 6 shows that the outflows that widen the radial velocity histograms in a given radial bin are primarily hot gas in the higher-mass halo (red filled circles), but primarily cold gas in the lower-mass halo (open light blue triangles). This is because a higher mass loading factor for the wind leads to more efficient radiative cooling (Thompson et al. 2016), and the lower-mass halo’s wind is initialized with a higher mass loading factor than the higher-mass halo. Again, the cold gas IQRs are more time-variant than the hot gas, which indicates that cold gas

flows are more time-variant not only in their medians but also in the range of radial velocities present in a given radial bin. Whereas the lower-mass halo has smaller range of radial velocities than the higher-mass halo when all gas is considered (top-right panel), this is no longer true when the gas is split by temperature — the cold gas in the lower-mass halo (light blue open triangles) shows a wider range of velocities at a given radius than either the hot or the cold gas in the higher-mass halo (circles), while the hot gas in the lower-mass halo (orange filled triangles) has the smallest range of velocities at a given radius out of all temperatures of gas in both halos.

3.4 Radial Turbulence Distributions

We investigated the turbulent pressure in Figure 5, but exploring the tangential velocity distributions, which can be considered a proxy for the turbulent velocity, and especially the temperature of the gas contributing to the tangential velocity, will reveal how the gas produces the turbulent velocity. We calculate the tangential velocity as the average of v_{θ} and v_{ϕ} , as above. Figure 7 shows the distribution of the IQRs of the tangential velocity with galactocentric ra-

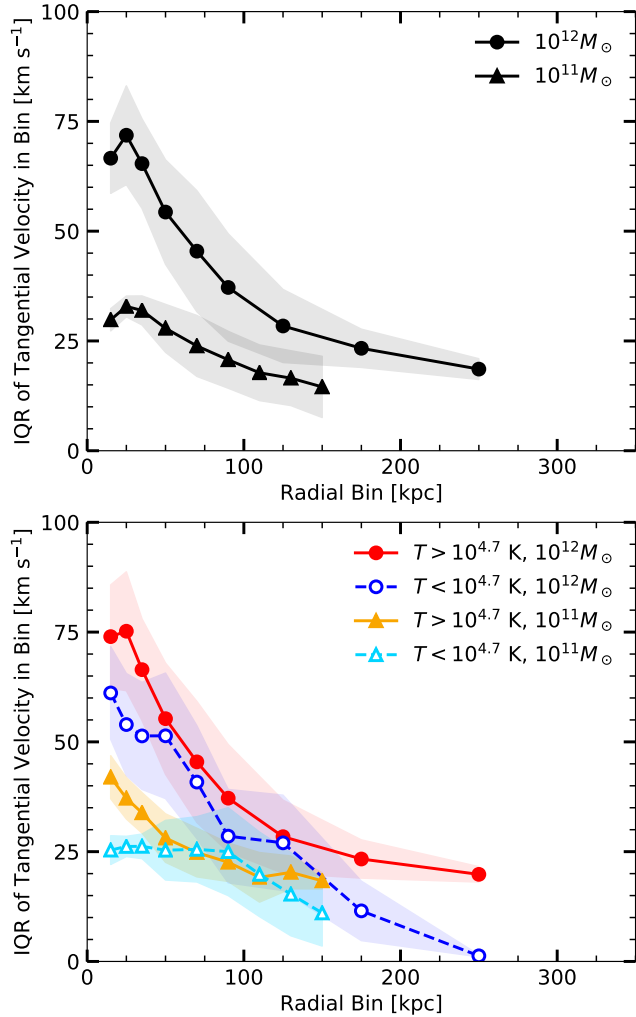


Figure 7. The time-averaged IQR of the tangential velocity as a function of radius for both the $10^{12}M_{\odot}$ (circles) and $10^{11}M_{\odot}$ halos. Top panel shows tangential velocities for all gas in each simulation, while bottom panel shows the IQR of the tangential velocity histograms when the gas is first separated by temperature at $T = 10^{4.7}$ K (hot: red and orange filled symbols; cold: light and dark blue open symbols). Shaded regions around curves indicate the one standard deviation time variance of the values. Note that the values in the top panel are the averages of the bottom panel only when weighted by the mass of gas in each temperature phase.

dius, for all gas in the top panel and with gas split into hot ($T > 10^{4.7}$ K, filled red and orange) and cold ($T < 10^{4.7}$ K, open light and dark blue) in the bottom panel, for both the higher-mass halo (circles) and the lower-mass halo (triangles). Because the medians of the v_{θ} and v_{ϕ} histograms are zero in all radial bins (see Figures 3 and 4), we show only the IQRs of the tangential velocity.

The higher-mass halo has a larger spread of tangential velocities in a given radial bin than the lower-mass halo, so it has a faster turbulent velocity. Both halos' tangential velocities decrease with increasing galactocentric radius, indicating that the turbulent velocity is higher in the central regions of the halo, but the higher-mass halo has a steeper slope and therefore a wider range of turbulent velocities throughout the halo. The bottom panel of Figure 7 show that in

the higher-mass halo, the hot and cold gases have similar turbulent velocities throughout much of the halo, but the cold gas has somewhat slower turbulence, and the difference between the gas temperatures becomes larger in the innermost and outermost radial bins. In the lower-mass halo, the cold gas has much lower turbulent speeds in the innermost radial bins than the hot gas, but the turbulent velocities in both the hot and cold gas are similar at larger radii. The similar turbulent velocities at both temperatures could be due to the fact that the gas is not as separated in temperature in the lower-mass halo as in the higher-mass halo, or could indicate that there is more mixing in the lower-mass halo that holds the turbulent velocity constant regardless of the temperature of the gas. Both temperatures of gas in the lower-mass halo have slower turbulent velocities than both temperatures of the higher-mass halo.

3.5 Hydrostatic Equilibrium

The smooth behavior of the pressure distributions and the fact they do not vary significantly over time leads to the idea that these halos are in hydrostatic equilibrium, where the thermal and turbulent pressures together work to support the gas against gravity. To explore this further, we define a parameter that measures the degree of hydrostatic equilibrium,

$$\text{HSE} = \left| \frac{\nabla_r P}{\rho \nabla_r \Phi} \right| \quad (2)$$

where Φ is the gravitational potential defined by the NFW dark matter halo, and ∇_r indicates the gradients of pressure and gravitational potential are taken in only the radial direction. If $\text{HSE} = 1$, the gas is in hydrostatic equilibrium, if $\text{HSE} < 1$, the gas is gravity-dominated and lacks the pressure support to hold it in place in the halo, so it may begin flowing inward, and if $\text{HSE} > 1$, the gas is over-pressurized and may be driving outflows.

We compute histograms of the HSE parameter in radial bins, as before, and Figure 8 shows the median (left panels) and IQR (right panels) of HSE as functions of radius, both for all gas (top panels) and gas that has been split into hot ($T > 10^{4.7}$ K) and cold ($T < 10^{4.7}$ K) gas (bottom panels), for both halos. The higher-mass halo is close to hydrostatic equilibrium in most radial bins, with a shallow decrease in HSE to slightly gravity-dominated in the outskirts of the halo (top left panel). The lower-mass halo is gravity-dominated throughout, but is closest to equilibrium at intermediate radial bins. As seen in other parameters above, the lower-mass halo's HSE parameter is more time-variable and also has a wider histogram of values at a given radial bin (top right panel). The pressure support for gas in the lower-mass halo is thus both more time-variable and also more variable at a given radius than in the higher-mass halo.

When the gas is split into low-temperature ($T < 10^{4.7}$ K, light and dark blue open symbols) and high-temperature ($T > 10^{4.7}$ K, red and orange filled symbols) regimes before the HSE histograms are calculated, then we see a striking difference in the pressure support. The hot gas in the higher-mass halo is much closer to equilibrium ($\text{HSE} \approx 1$) than the cold gas ($\text{HSE} \approx 0.1$), which is strongly gravity-dominated and explains the predominantly negative

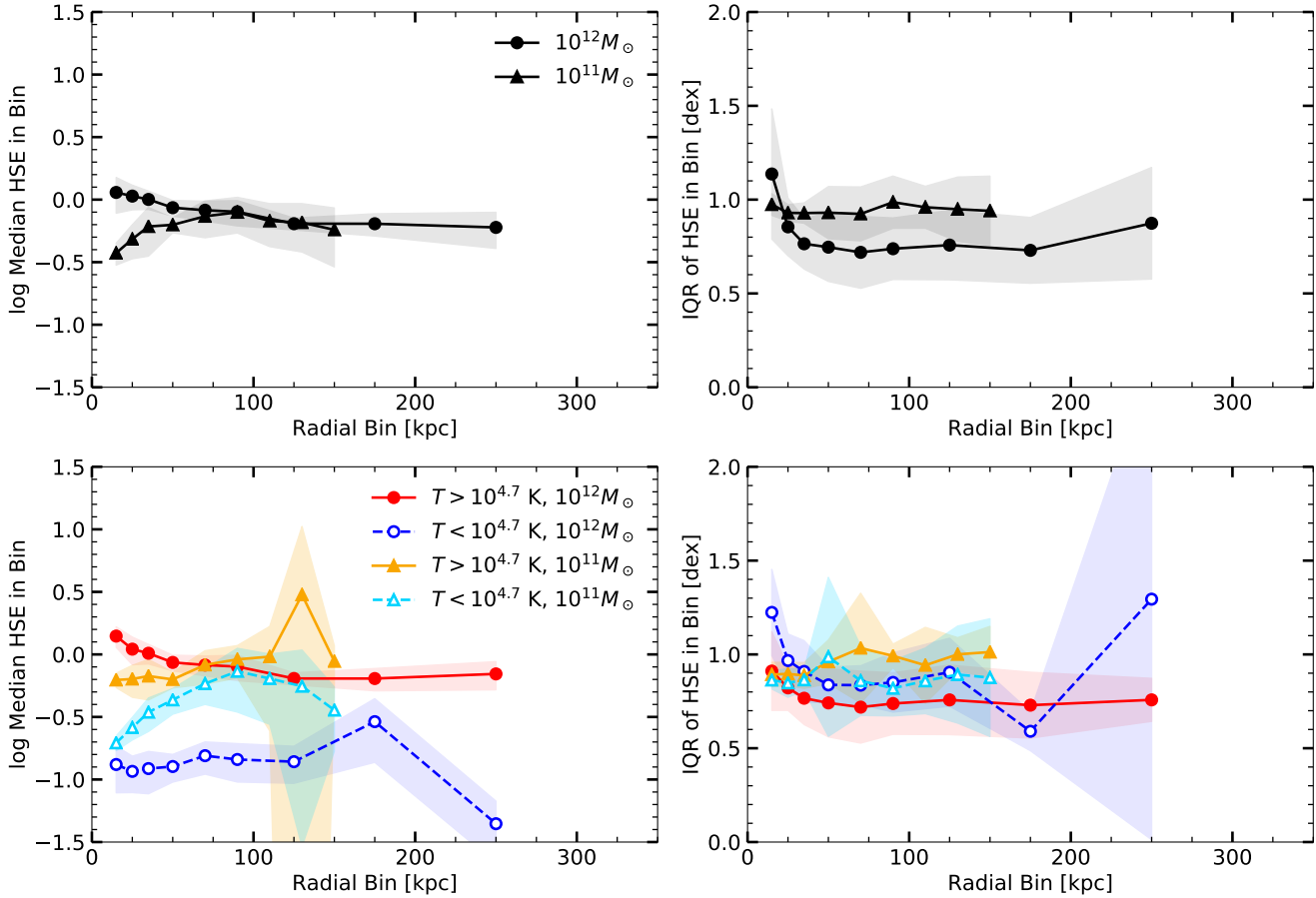


Figure 8. Left panels show the time-averaged median HSE (equation 2) as a function of radius for both the $10^{12} M_{\odot}$ (circles) and $10^{11} M_{\odot}$ halos. Right panels show the time-averaged IQR of the HSE histograms in both halos. Top panels show HSE for all gas in each simulation, while bottom panels show the median and IQR of the HSE histograms when the gas is first separated by temperature at $T = 10^{4.7} \text{ K}$. Shaded regions around curves indicate the one standard deviation time variance of the values. Note that the values in the top panels are the averages of the bottom panels only when weighted by the mass of gas in each temperature phase.

values for the radial velocity in the cold gas seen in Figure 6. In the lower-mass halo, the two gas temperatures have similar values of HSE at intermediate radii, but the hot gas is closer to equilibrium than the cold gas, especially in the inner regions of the halo where the cold gas is gravity-dominated. The IQR of HSE within each radial bin is typically somewhat larger for the lower-mass halo, but there is not a strong separation between the hot and cold gas within each halo. The colder gas in the higher-mass halo has weakly wider histograms at most radii while in the lower-mass halo, this is flipped, with the hotter gas having somewhat wider histograms within a given radial bin. There is a large time variance in the IQR of HSE for gas on both sides of the temperature cut, but the cold gas has a slightly more time-variable IQR in both halos than the hot gas.

These trends are not unexpected, as the cold gas will have a lower thermal pressure than the hot gas. However, thermal pressure is not the only source of pressure support — we have seen above that while the turbulent pressure is not as strong as the thermal pressure when considering all gas in the halo (Figure 5), it could make a significant difference to the overall pressure support when the gas is split by temperature. We recalculate HSE by now replacing P in equation (2) with $P_{\text{therm}} + P_{\text{turb}}$, the sum of thermal

and turbulent pressures. The new HSE median (left panels) and IQR (right panels) values are plotted in Figure 9 for all gas (top panels) and temperature-split gas (bottom panels), for both halos.

The median values of HSE shift upward regardless of which gas is being considered, especially in the innermost regions of the halos where the turbulent pressure is largest. The higher-mass halo (circles) is now more over-pressurized in the inner regions of the halo, which is to be expected due to the strong outflows from the galaxy at the center, but is in rough hydrostatic equilibrium with $\text{HSE} \approx 1$ in the outer regions of the halo, no longer slightly under-pressurized as in Figure 8. The lower-mass halo (triangles) has shifted from being gravity-dominated everywhere to being slightly over-pressurized everywhere — turbulent pressure support is clearly very important to determine if the halo is predominantly outflowing or inflowing. The lower-mass halo still has a larger time-variance in the median HSE, and also a larger IQR of HSE at all radii except the smallest radial bin, than the higher-mass halo.

When the gas is first split by temperature before calculating HSE, the hot gas is still more pressurized in both halos than the cold gas in most radial bins, with the exception of some intermediate radial bins in both halos, but the cold

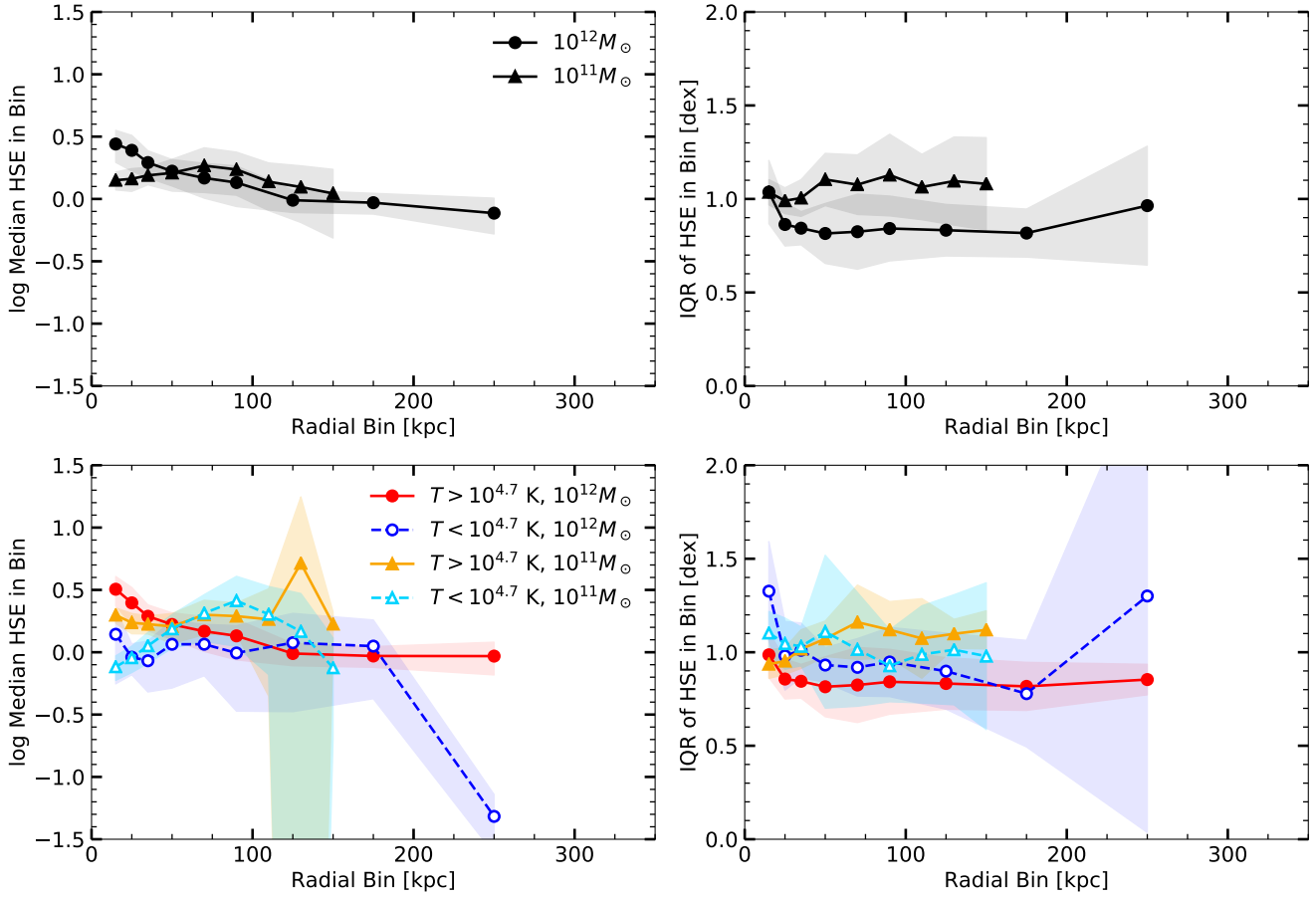


Figure 9. Left panels show the time-averaged median HSE (equation 2), now computed using the sum of thermal and turbulent pressures, as a function of radius for both the $10^{12} M_{\odot}$ (circles) and $10^{11} M_{\odot}$ halos. Right panels show the time-averaged IQR of the HSE histograms in both halos. Top panels show HSE for all gas in each simulation, while bottom panels show the median and IQR of the HSE histograms when the gas is first separated by temperature at $T = 10^{4.7}$ K. Shaded regions around curves indicate the one standard deviation time variance of the values. Note that the values in the top panels are the averages of the bottom panels only when weighted by the mass of gas in each temperature phase.

gas in both halos has shifted to significantly higher values of HSE. This is expected because the hot gas has a higher thermal pressure due to its temperature, but both temperatures of gas have similar turbulent properties (see Figure 7) so the sum of the thermal and turbulent pressures is larger for the hotter gas in most radial bins. The higher value of HSE for the cold gas in intermediate radial bins in the lower-mass halo can be understood because the turbulent velocities of the cold gas in the lower-mass halo are larger than the hot gas for the few bins where the HSE parameter is also larger, so the inclusion of the turbulent pressure in calculating HSE allows the cold gas to be more over-pressured than the hot gas in intermediate radial bins. In addition, the temperatures of the gas on either side of the temperature divide in the lower-mass halo are not very strongly separated, so the thermal pressures are similar for the hot and cold gas. In the higher-mass halo, the temperature difference between the hot and cold gas is much larger, so the cold gas is also much denser than the hot gas, so the cold gas can have a similar sum of thermal and turbulent pressures as the hot gas despite the fact that the turbulent velocity is somewhat higher in the hot gas. The general trends in the HSE IQR

values for the hot and cold gas are similar here as in Figure 8 for just the thermal pressure.

The inclusion of turbulent pressure in calculating the full pressure support for the halo is crucial, especially for the pressure support of the cold gas. The hot gas’s pressure support comes primarily from its thermal pressure, as seen in Figure 8, but the cold gas’s pressure support is provided primarily by its turbulent pressure, as seen in Figure 9. In addition, only the higher-mass halo is in a steady state of pressure equilibrium at a majority of radii, which is primarily provided by the hot gas (which also dominates the mass of the higher-mass halo). The lower-mass halo is not in equilibrium and is instead over-pressurized and driving outflows at all radii, but with a high level of time-variance. Note that the histograms of HSE within each radial bin are volume histograms, while the histograms of radial velocity (see Figure 6) are mass histograms. Therefore, while it appears the majority of the volume of each halo is over-pressurized, the majority of the mass in each halo is slowly inflowing.

4 DISCUSSION

4.1 Dependence of CGM Properties on Halo Mass

We have performed a careful analysis of the properties of CGM gas within two simulations of galaxies hosted by $10^{12}M_{\odot}$ and $10^{11}M_{\odot}$ halos, and found a number of differences in the CGM between halos of these different masses. The lower-mass halo has been more time-variant and had a wider range of values within each radial bin in its thermal and turbulent pressure distributions (Figure 5) and its degree of hydrostatic equilibrium (both with and without turbulent pressure, Figures 8 and 9). This is despite the lower radial velocities that were set as initial conditions for the outflow in this halo. The CGM of halos of mass $\sim 10^{11}M_{\odot}$ appears to be more dynamic than that of higher-mass halos. Combined with the fact that the gas in this halo is not in hydrostatic equilibrium, regardless of whether only the hot or cold gas is considered, forwards a picture in which there is no steady-state of the CGM for low-mass halos.

On the other hand, the $10^{12}M_{\odot}$ halo follows the trends expected for a classical “hot halo” in pressure equilibrium. The pressure distribution is well-behaved, is neither very time-variant nor are there a large range of pressures within a given radial bin. The hot gas is roughly in thermal pressure equilibrium at most large radii, with perhaps some outflows near the central galaxy, while the cold gas is generally turbulent pressure-supported in a volume-averaged sense.

The majority of the cold gas mass in the higher-mass halo is inflowing, while the hot gas is outflowing near the galaxy at the center but otherwise mostly static in the halo, a picture also expected for a hot gas halo from which cold clouds can condense to “rain” onto the central galaxy (Pizzoloto & Soker 2005; Soker 2010; Gaspari et al. 2012). The lower-mass halo is reversed, with the majority of the cold gas mass outflowing and the hot gas mass inflowing.

The CGM of lower-mass halos should certainly not be considered the same way as higher-mass halo. It is dynamic and not in equilibrium, nor is there cold gas condensing out of a hot medium. It changes drastically as the galaxy evolves and is dominated by bulk flows, not thermal gas properties.

4.2 Implications for Small-Box CGM Simulations

The well-behaved and expected nature of the CGM of the $10^{12}M_{\odot}$ halo, i.e. a static hot halo in pressure equilibrium from which cold clouds condense from thermal instabilities, allows for easier modeling of a small patch of the CGM. Close to the central galaxy, there may be additional complications from strong galactic outflows, but initializing a small-box simulation would require only information about the pressure support of the gas and its turbulent properties. Such small-box simulations would be invaluable for exploring how thermal instability proceeds in the outer CGM of massive galaxies and the formation of cold gas.

The more time-variant and non-equilibrium nature of the $10^{11}M_{\odot}$ halo’s CGM creates a more complicated problem for small-box simulators. The CGM is dominated by bulk flows, both in and out, and there is not a strong difference between the hot and cold gas phases. There is significant turbulent support and the turbulence itself is the only well-behaved quantity. Both hot and cold gas can be both

outflowing and inflowing, so initializing a small box to represent a patch of a lower-mass galaxy’s CGM would require a careful choice of what stage of the CGM’s evolution will be simulated. There are significant asymmetries that develop in the lower-mass halo, even in idealized, spherically-symmetric simulations, so a suite of small-box simulations at many locations within the halo would be necessary to understand the small-scale physical processes occurring everywhere within the CGM of a low-mass galaxy.

4.3 Dependence on Feedback Parameters

In addition to the reference set of wind parameters for the $10^{11}M_{\odot}$ halo, we also examined three other combinations of wind speed v_w and mass-loading η : one with the same mass-loading factor as our reference simulation ($\eta = 5$) but with a lower $v_w^2 = v_{\text{esc}}^2$ (instead of the $v_w^2 = 3v_{\text{esc}}^2$ of our reference simulation), and two with a lower mass-loading factor of $\eta = 0.3$, with $v_w^2 = 4.5v_{\text{esc}}^2$ or $v_w^2 = 9v_{\text{esc}}^2$. All other initial conditions were kept the same, and we calculated histograms within radial bins of the pressures, radial velocities, and HSE parameter (equation 2) using the sum of thermal and turbulent pressures, and calculated the time-averaged median and IQR of these histograms, as before.

Figure 10 shows the median of the thermal (black filled points) and turbulent (green open points) pressures in the left panel, and the IQR of the histograms within each radial bin in the right panel, for all four $10^{11}M_{\odot}$ simulations. Our reference simulation is represented by triangles, while the other three are represented by squares, diamonds, or hexagons, as labeled in the figure. We neglect shading around the curves indicating time variance for ease of plot reading. As before, we see the thermal pressures are typically larger than the turbulent pressures, while the turbulent pressures have a wider histogram within a given radial bin.

There is not a large difference in the medians or IQRs of the pressures between different sets of wind parameters, with the exception of the one simulation with $\eta = 5$ and $v_w^2 = v_{\text{esc}}^2$ (squares), which has the lowest wind speed out of the sets of wind parameters explored here. Due to this low wind speed, the wind does not travel very far into the halo, and the CGM is highly asymmetric as the wind can push through the CGM only through the least dense regions. The larger radial bins for this simulation thus do not contain any wind material at all, only the gas that is accreting onto the halo, which is both thermally under-pressurized and has very low turbulence. Therefore, the only part of this halo in which outflows are present, which is the only part that should be compared to the other simulations, is the innermost four radial bins. Within those bins, there is no difference in the thermal pressure median between this set of wind parameters and any of the others, although this simulation has somewhat lower turbulent pressures than the rest. The transition from wind to accretion at intermediate radii in this simulation also creates the larger IQRs of both thermal and turbulent pressures in this simulation compared to the others.

The only other set of wind parameters that stands out is that with $\eta = 0.3$ and $v_w^2 = 4.5v_{\text{esc}}^2$ (diamonds), which has somewhat lower thermal pressure in the outskirts of the halo and significantly larger turbulent pressure IQR at large radii

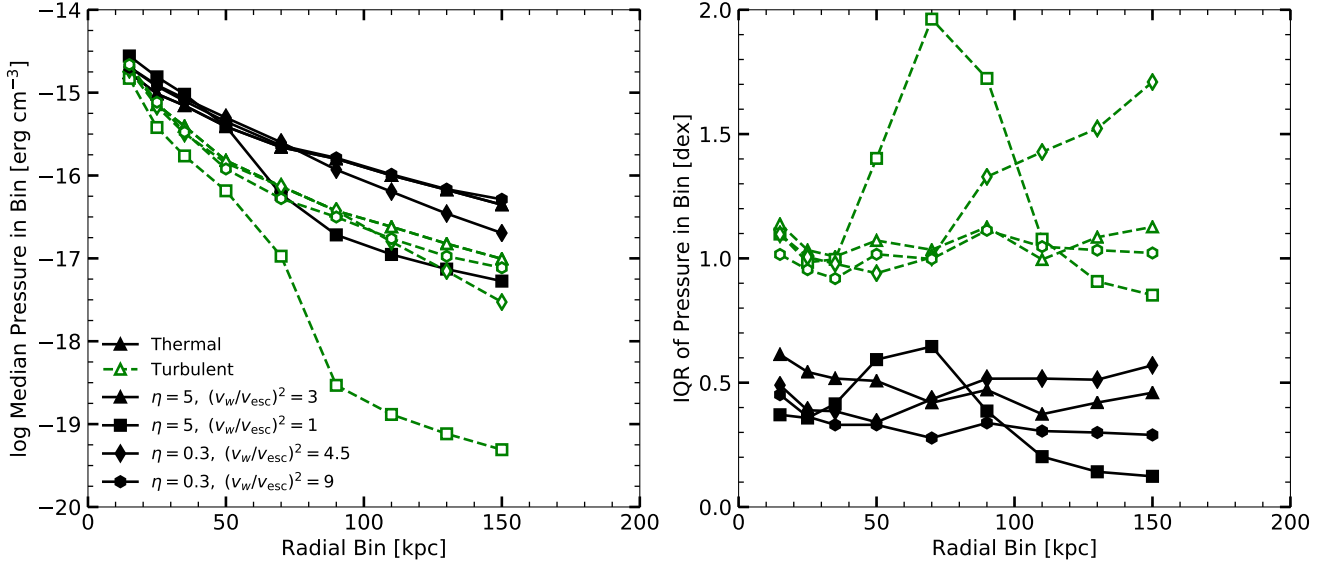


Figure 10. Left panel shows the time-averaged median thermal (black filled symbols) and turbulent (open green symbols) pressures as functions of radius for $10^{11} M_{\odot}$ halos with different sets of wind parameters: the reference case with $\eta = 5$ and $v_w^2 = 3v_{\text{esc}}^2$ (triangles), a case with $\eta = 5$ and $v_w^2 = v_{\text{esc}}^2$ (squares), a case with $\eta = 0.3$ and $v_w^2 = 4.5v_{\text{esc}}^2$ (diamonds), and a case with $\eta = 0.3$ and $v_w^2 = 9v_{\text{esc}}^2$ (hexagons). Right panel shows the time-averaged IQR for both types of pressure in all simulations.

than the other simulations. In this simulation, the outflows tend to travel to about the largest radial bin before falling back toward the galaxy. There is therefore a combination of outflows and accretion in the largest radial bins, which reduces the thermal pressure, and also drastically increases the range of turbulence in a given radial bin, as the outflows have significant turbulence while the accretion does not.

Next, we consider radial velocities within these four simulations. Figure 11 shows the median (left panels) and IQR (right panels) of the radial velocity in these four simulations for all gas (top panels) and gas split into hot and cold (bottom panels) at the same dividing temperature as above. All sets of wind parameters produce an inflow-dominated halo, similar to the reference case. The simulation with $\eta = 5$ and $v_w^2 = v_{\text{esc}}^2$ (squares) has faster inflows at large radii than the other simulations for the same reason as it is under-pressurized: the outflows do not travel to large radii so there is only the cosmological accretion at these large radii. Similarly, the simulation with $\eta = 0.3$ and $v_w^2 = 4.5v_{\text{esc}}^2$ (diamonds) is slightly more inflow-dominated than the others, again because the outflows in this simulation do not travel all the way to the edge of the simulation domain, and end up returning to the central galaxy. All simulations have similar IQRs of radial velocity when all gas is considered.

When the gas is split by temperature, the general trend of the hot gas entirely inflowing while the cold gas may be weakly outflowing at some radii is observed for all simulations as in the reference case, but the biggest difference between the simulations is the radius at which the cold gas has $v_r \geq 0 \text{ km s}^{-1}$. The reference simulation (triangles) has the strongest outflows, while the one with the slowest outflows (squares) has cold gas with $v_r \geq 0 \text{ km s}^{-1}$ only at the smallest radii. The other two sets of wind parameters (diamonds and hexagons) have cold gas closest to outflowing velocities at intermediate radii. The reference simulation has the largest radial velocity IQR of both hot and cold gas,

indicating that it contains the most gas traveling at different velocities within a given radial bin. The other simulations typically have higher velocity IQRs in the cold gas at small radii that transitions to higher velocity IQRs in the hot gas at large radii. The hot gas velocity IQRs follow similar distributions in all simulations, again with the exception of that with the slowest outflows that is mostly dominated by inflows everywhere within the halo.

Finally, we consider the degree of hydrostatic equilibrium in the halos with these different wind parameters. Figure 12 shows the median (left panels) and IQR (right panels) of the HSE parameters (equation 2) calculated using the sum of thermal and turbulent pressures for the gas in all $10^{11} M_{\odot}$ simulations, for all gas (top panels) and gas that is split in temperature into hot and cold (bottom panels).

The simulation with the fastest wind speed (hexagons) follows a similar distribution of HSE median and IQR as the reference simulation, both when all gas is considered and when gas is split by temperature, with the one exception that there is a higher degree of pressure support in this simulation with fast wind at small radii than in the reference simulation. All gas, hot gas, and cold gas all have a higher value of median HSE at small radii in this simulation than the reference, which is likely due to the fast winds shock-heating to a higher temperature, and therefore having a higher level of thermal support, than the relatively slower winds in the reference simulation. In addition, this simulation generates more turbulence than the reference due to the fast winds, which also increases the level of support in the cold gas.

The simulation with the lowest wind speed (squares) is very under-pressurized everywhere in the halo, and also has the smallest range of HSE values within a given radial bin, as indicated by the small IQR values. Because this halo is dominated by cold accreting gas, it is expected that there is very little, if any, pressure support. When the gas is split

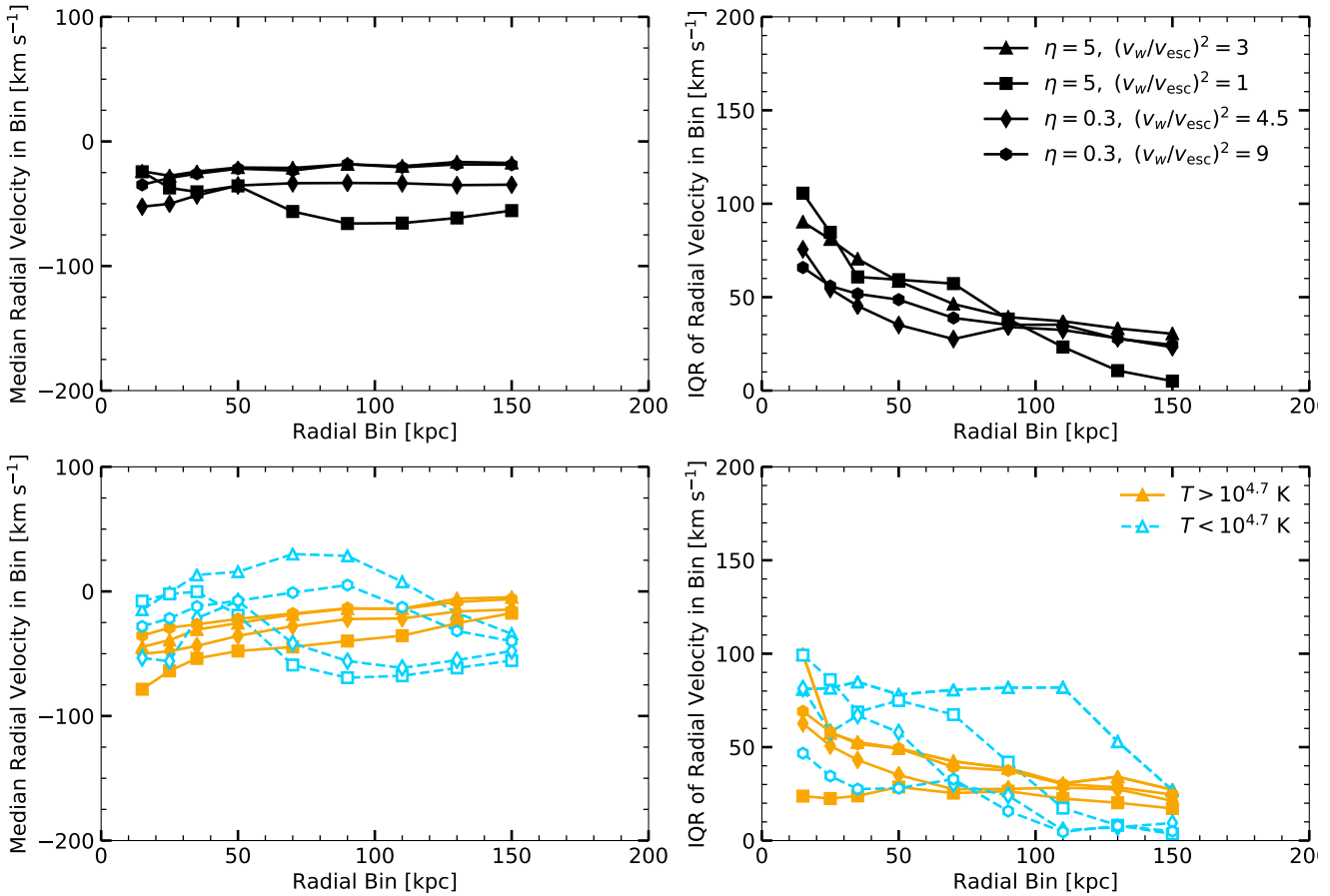


Figure 11. Left panels show the time-averaged median radial velocity as a function of radius for all $10^{11} M_{\odot}$ halos with different sets of wind parameters: the reference case with $\eta = 5$ and $v_w^2 = 3v_{\text{esc}}^2$ (triangles), a case with $\eta = 5$ and $v_w^2 = v_{\text{esc}}^2$ (squares), a case with $\eta = 0.3$ and $v_w^2 = 4.5v_{\text{esc}}^2$ (diamonds), and a case with $\eta = 0.3$ and $v_w^2 = 9v_{\text{esc}}^2$ (hexagons). Right panels show the time-averaged IQR of the radial velocity histograms in all simulations. Top panels show radial velocities for all gas in each simulation, while bottom panels show the median and IQR of the radial velocity histograms when the gas is first separated by temperature at $T = 10^{4.7}$ K. Note that the values in the top panels are the averages of the bottom panels only when weighted by the mass of gas in each temperature phase.

into hot and cold, the cold gas has little pressure support due to the low level of turbulence that the slow wind induces in this halo, but the hot gas is over-pressurized in the outskirts of the halo. This is because the only hot gas that travels to the outer edges of the halo (which is small by mass compared to the cold gas) does so because it passes through a low-density channel where it does not lose much energy to expanding against the gas in the halo and can maintain its high pressure.

The simulation with $\eta = 0.3$ and $v_w^2 = 4.5v_{\text{esc}}^2$ (diamonds) shows a similar behavior as the reference solution in the HSE median trends of all gas, hot gas, and cold gas, but scaled down, excluding the outer edges of the halo where the wind in this simulation only sporadically reaches. This set of wind parameters is analogous to the reference simulation, but with the mass-loading factor and energetics of the wind scaled down. This produces a CGM that is similar to the reference simulation, but has somewhat less pressure support in all phases of gas, as expected from a somewhat less energetic wind.

Overall, we find that changing the wind parameters has the largest effect on the pressure support of the gas in the CGM. We reiterate the conclusion from §4.2 that the lower-

mass halo is not only more dynamic and further from equilibrium than the higher-mass halo, but its support is also strongly dependent on the properties of the wind, which only serves to make initializing small-box simulations of the CGM in low-mass halos more difficult.

5 SUMMARY AND CONCLUSIONS

We have characterized the circumgalactic medium of two simulated galaxy halos of dark matter mass $10^{12} M_{\odot}$ and $10^{11} M_{\odot}$. These simulations are idealized and spherically symmetric, of isolated galaxies, and do not model the galaxy itself nor any cosmological evolution (other than a constant spherical accretion), but are high-resolution and include radiative cooling in photoionization equilibrium and galactic winds parameterized by a mass loading factor and a wind velocity.

Our main findings are as follows:

- (i) The histogram of thermal pressure of all cells within radial bins in the CGM are well-defined by roughly log-normal distributions that promote characterization by a median and interquartile range of the middle 60% of the

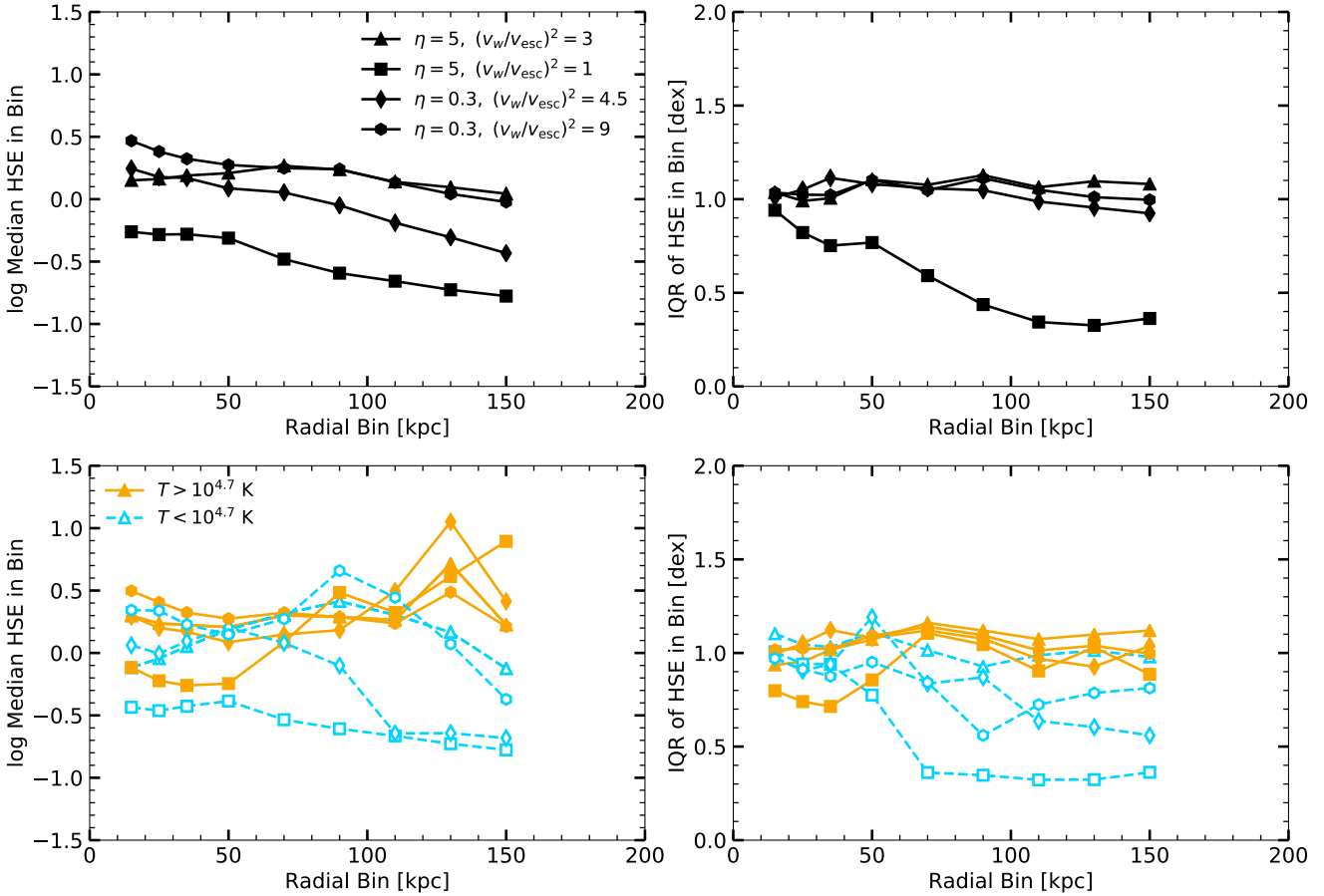


Figure 12. Left panels show the time-averaged median HSE (equation 2), computed using the sum of thermal and turbulent pressures, as a function of radius for $10^{11} M_{\odot}$ halos with different sets of wind parameters: the reference case with $\eta = 5$ and $v_w^2 = 3v_{\text{esc}}^2$ (triangles), a case with $\eta = 5$ and $v_w^2 = v_{\text{esc}}^2$ (squares), a case with $\eta = 0.3$ and $v_w^2 = 4.5v_{\text{esc}}^2$ (diamonds), and a case with $\eta = 0.3$ and $v_w^2 = 9v_{\text{esc}}^2$ (hexagons). Right panels show the time-averaged IQR of the HSE histograms in all simulations. Top panels show HSE for all gas in each simulation, while bottom panels show the median and IQR of the HSE histograms when the gas is first separated by temperature at $T = 10^{4.7}$ K. Note that the values in the top panels are the averages of the bottom panels only when weighted by the mass of gas in each temperature phase.

histogram. Higher-mass halos have narrower histograms of thermal pressure within any given radial bin than lower-mass halos, and are also less time-variable.

(ii) Histograms of radial and angular velocities of all cells within radial bins show that velocities tangential to the radial direction are good tracers of turbulence, while the radial velocity histogram contains information of inflows, outflows, and turbulence. The velocity of both outflows and turbulence is larger in higher-mass halos; outflows are faster by design and seed faster turbulence.

(iii) Both high- and low-mass halos contain predominantly inflowing gas when all gas is considered, but when the gas is split into high temperature ($T > 10^{4.7}$ K) and low temperature ($T < 10^{4.7}$ K), then cold gas in high-mass halos is inflowing while cold gas in low-mass halos is outflowing, and hot gas in high-mass halos is static while hot gas in low-mass halos is inflowing.

(iv) When only thermal pressure is considered, the high-mass halo is close to hydrostatic equilibrium but slightly under-pressurized. The hot gas provides nearly all of the thermal pressure support while the cold gas is extremely under-pressurized. When turbulent pressure is included, the

high-mass halo is in hydrostatic equilibrium at nearly all radii, but over-pressurized (likely due to outflows) at small radii, and both the hot and cold gas are roughly in equilibrium. The over-pressurization at small radii is present only in the hot gas, indicating that only the hot gas is outflowing.

(v) The low-mass halo is under-pressurized at small radii and close to hydrostatic equilibrium, but still slightly under-pressurized, at larger radii, when only thermal pressure is considered for support. Both the hot and cold gas are under-pressurized, with the cold gas being severely under-pressurized at small radii. When turbulent pressure is included, the entire low-mass halo becomes slightly over-pressurized, with most of the pressure support at small radii being provided by the hot gas, just as in the higher-mass halo when the sum of thermal and turbulent pressures provides the support.

(vi) Variations in the mass loading and wind velocity produce the largest effects on the degree of pressure support in the low-mass halo. Galactic winds with low wind speeds or low mass loading factors tend to produce more under-pressurized and inflow-dominated CGM than those with higher mass loading or wind speed.

The high-mass halo's CGM follows the expected picture of a hot gas halo in pressure equilibrium out of which cold gas condenses and rains onto the galaxy, but the low-mass halo does not have a hot gas halo, is not in pressure equilibrium, and does not show any signatures of condensing cold gas. In addition, the properties of the low-mass halo are dependent on the galactic wind parameters. These findings imply that simulators who wish to perform small-box simulations of a patch of the CGM in order to accurately trace thermal instability and condensation at high resolution must make careful decisions about how to initialize their simulations, as the properties of any given patch of the CGM in a low-mass halo vary significantly with time, location in the halo, and galactic wind properties, and the CGM may have large-scale asymmetries driven by the wind escaping through areas of lowest density. We have shown that there is no such thing as an "average" CGM in low-mass halos.

The idealized nature of these simulations is useful for understanding the physical processes that drive the evolution of the CGM, but there are many areas for improvement. Cold cosmological accretion is typically not perfectly spherically-symmetric, but may pierce through the CGM in filaments. Galactic winds flowing from a disk are not expected to be spherically-symmetric, but instead biconical. The typical galaxy goes through many mergers during its evolution that may drastically change its CGM. In any case, the multiphase nature of the CGM requires careful analysis of not just the average properties of all gas, but the properties of each individual phase. This paper provides a component of a physically-motivated characterization of the complete nature of the CGM.

ACKNOWLEDGMENTS

This work was initiated as a project for the Kavli Summer Program in Astrophysics held at the Center for Computational Astrophysics of the Flatiron Institute in 2018. The program was co-funded by the Kavli Foundation and the Simons Foundation. We thank them for their generous support.

REFERENCES

- Anderson, M. E., & Bregman, J. N. 2010, *ApJ*, 714, 320
 Anderson, M. E., Bregman, J. N., & Dai, X. 2013, *ApJ*, 762, 106
 Anglés-Alcázar, D., Davé, R., Özel, F., & Oppenheimer, B. D. 2014, *ApJ*, 782, 84
 Bordoloi, R., Tumlinson, J., Werk, J. K., et al. 2014, *ApJ*, 796, 136
 Borthakur, S., Heckman, T., Tumlinson, J., et al. 2015, *ApJ*, 813, 46
 Chisholm, J., Tremonti, C., & Leitherer, C. 2018, *MNRAS*,
 Christensen, C. R., Dave, R., Brooks, A., Quinn, T., & Shen, S. 2018, arXiv:1808.07872
 Ferrara, A., & Scannapieco, E. 2016, *ApJ*, 833, 46
 Fielding, D., Quataert, E., McCourt, M., & Thompson, T. A. 2017, *MNRAS*, 466, 3810
 Gaspari, M., Ruszkowski, M., & Sharma, P. 2012, *ApJ*, 746, 94
 Gronke, M., & Oh, S. P. 2018, *MNRAS*, 480, L111
 Gupta, A., Mathur, S., Krongold, Y., Nicastro, F., & Galeazzi, M. 2012, *ApJL*, 756, L8
 Haardt, F., & Madau, P. 2001, *Clusters of Galaxies and the High Redshift Universe Observed in X-rays*, 64
 Heckman, T. M., Alexandroff, R. M., Borthakur, S., Overzier, R., & Leitherer, C. 2015, *ApJ*, 809, 147
 Henden, N. A., Puchwein, E., Shen, S., & Sijacki, D. 2018, *MNRAS*, 479, 5385
 Hopkins, P. F., Kereš, D., Oñorbe, J., et al. 2014, *MNRAS*, 445, 581
 Keeney, B. A., Stocke, J. T., Danforth, C. W., et al. 2017, *ApJS*, 230, 6
 Liang, C. J., & Remming, I. S. 2018, arXiv:1806.10688
 McCourt, M., Sharma, P., Quataert, E., & Parrish, I. J. 2012, *MNRAS*, 419, 3319
 Muratov, A. L., Kereš, D., Faucher-Giguère, C.-A., et al. 2015, *MNRAS*, 454, 2691
 Muzahid, S., Kacprzak, G. G., Churchill, C. W., et al. 2015, *ApJ*, 811, 132
 Muzahid, S., Fonseca, G., Roberts, A., et al. 2018, *MNRAS*, 476, 4965
 Navarro, J. F., Frenk, C. S., & White, S. D. M. 1997, *ApJ*, 490, 493
 Peeples, M. S., Werk, J. K., Tumlinson, J., et al. 2014, *ApJ*, 786, 54
 Pillepich, A., Nelson, D., Hernquist, L., et al. 2018, *MNRAS*, 475, 648
 Pizzolato, F., & Soker, N. 2005, *ApJ*, 632, 821
 Prochaska, J. X., Werk, J. K., Worseck, G., et al. 2017, *ApJ*, 837, 169
 Rahmati, A., Schaye, J., Crain, R. A., et al. 2016, *MNRAS*, 459, 310
 Rudie, G. C., Steidel, C. C., Trainor, R. F., et al. 2012, *ApJ*, 750, 67
 Sarkar, K. C., Nath, B. B., Sharma, P., & Shchekinov, Y. 2015, *MNRAS*, 448, 328
 Sharma, P., McCourt, M., Quataert, E., & Parrish, I. J. 2012, *MNRAS*, 420, 3174
 Soker, N. 2010, *MNRAS*, 407, 2355
 Thompson, T. A., Quataert, E., Zhang, D., & Weinberg, D. H. 2016, *MNRAS*, 455, 1830
 Tumlinson, J., Thom, C., Werk, J. K., et al. 2013, *ApJ*, 777, 59
 Tumlinson, J., Peeples, M. S., & Werk, J. K. 2017, *ARAA*, 55, 389
 Turk, M. J., Smith, B. D., Oishi, J. S., et al. 2011, *ApJS*, 192, 9
 Voit, G. M., Meece, G., Li, Y., et al. 2017, *ApJ*, 845, 80
 Voit, G. M. 2018, arXiv:1803.06036
 Werk, J. K., Prochaska, J. X., Tumlinson, J., et al. 2014, *ApJ*, 792, 8